J Mater Sci (2022) 57:10233–10241

Electronic materials

Ultrahigh electrostrains of lead-free (Ba,Ca)(Ti,Zr)O_3 piezoelectric ceramics via defect engineering

Xueshuo Li[1], Jian Fu[1,*], Yuhan Yang[1], Zhenchang Li[1], Wenxuan Song[1], and Ruzhong Zuo[2,*]

[1] School of Materials Science and Engineering, Hefei University of Technology, Hefei 230009, People's Republic of China
[2] Center for Advanced Ceramics, School of Materials Science and Engineering, Anhui Polytechnic University, Wuhu 241000, People's Republic of China

Received: 10 February 2022
Accepted: 9 April 2022
Published online: 19 May 2022

ABSTRACT

Piezoelectric ceramics with large electric field-induced strain are of great importance for actuator applications. Unfortunately, $BaTiO_3$-based ceramics usually exhibit relatively low strain in spite of their high large-signal piezoelectric coefficient d_{33}*. In this study, an ultrahigh electrostrain with a value of ~ 0.242% (d_{33}* = 1210 pm/V) at 2 kV/mm is achieved in MnO_2-doped (Ba,Ca)(Ti,Zr)O_3 (BCTZ)-based lead-free piezoelectric ceramics via defect engineering, which is ~ 82% higher than that of the undoped sample. Detailed structural analysis in combination with various electrical property measurements revealed that such an ultrahigh strain should be attributed to the internal bias field E_i as a result of defect dipoles between the acceptor Mn ions and the oxygen vacancies, accompanied by the recoverable strain and the enhanced asymmetry of strain vs. electric field curve. The results demonstrate that the studied compositions might have great potential for applications of lead-free actuator piezoelectric ceramics.

Introduction

Recently, lead-free ceramics with large strains that can be suitable for ceramic actuator applications have attracted much attention. Among the reported lead-free counterparts, $(Bi_{0.5}Na_{0.5})TiO_3$ (BNT)-based systems usually exhibit large electric field-induced strains with the value of 0.3–0.5%. However, the electric field required for achieving large strains is very high, leading to the extremely low large-signal piezoelectric coefficient d_{33}* (S_{max}/E_{max}) in these systems [1–4].

$BaTiO_3$ (BT)-based piezoelectric ceramics have been considered as one of the most promising lead-free candidates because these materials exhibit not only the obvious advantages of low cost and easy processing, but also excellent piezoelectric coefficient

Handling Editor: Till Froemling.

Address correspondence to E-mail: fujian0715@126.com; zuoruzhong@ahpu.edu.cn

https://doi.org/10.1007/s10853-022-07281-x

(d_{33}) near the multiple phase coexisted boundary. The latter case is believed to be beneficial to obtain high strain by taking into account of the strain contribution in piezoelectric ceramics [5–10]. Unfortunately, only relatively low strain values can be observed in these modified BT-based piezoelectric ceramics. It is found that in many BT-based piezoelectric ceramics, large d_{33}* value can be only achieved in an extremely low electric field range, above which the d_{33}* value shows an obvious decrease, leading to the low strain value [11–18]. This should be attributed to a fact that the electric field needed to switch the ferroelectric domains in BT-based systems is much lower than that of other types of piezoelectric ceramics such as $Pb(Zr,Ti)O_3$ (PZT) and $(Na,K)NbO_3$ (NKN) systems [19].

Acceptor doping is an effective strategy to modify the ferroelectric and piezoelectric properties of piezoelectric ceramics via the defect dipoles between the negatively charged defects (i.e., impurity defects) and positively charged defects (i.e., oxygen vacancy) [20–23]. The defect dipole is believed to cooperatively align the direction of spontaneous polarization (Ps) and can provide a restoring force to recover the switched polarization, leading to the reversible domain switching and recoverable electrostrain [24–29]. This would be beneficial for achieving large strain in BT-based ceramics. In the present study, lead-free $(Ba_{0.865}Ca_{0.135})(Ti_{0.91}Zr_{0.09})O_3$ (BCTZ) + x mol% MnO_2 (x = 0–1.25) system was constructed. The selected BCTZ composition is located at the tetragonal-rich side of orthorhombic–tetragonal phase boundary [10], which is conductive to achieve the hardening effect. A small amount of MnO_2 was added to produce the oxygen vacancies due to the charge compensation. The influence of MnO_2 on the phase structure and various electrical properties, particularly, the strain properties was investigated in detail.

Experimental procedure

The BCTZ ceramic was prepared by a conventional solid-state reaction method by using high-purity raw materials. Barium carbonate ($BaCO_3$), calcium carbonate ($CaCO_3$), titanium dioxide (TiO_2) and zirconium dioxide (ZrO_2) (AR, Sinopharm Chemical Reagent Co., Ltd., CN) were used as the raw materials. All of the stoichiometric raw powders were mixed by planetary ball milling in ethanol for 4 h. After calcination at 1250 °C for 4 h, the calcined powders with different MnO_2 content (0–1.25 mol%) and 0.5 wt% polyvinyl butyral (PVB) were ball milled again for 6 h. The dried slurries were pressed into green pellets with a diameter of 10 mm and a thickness of 0.7–0.8 mm under a pressure of 150–200 MPa, and then sintered at 1320–1420 °C for 3 h in air.

The crystal structure of the as-sintered ceramic powders was examined by an X-ray diffractometer (XRD, D/MAX-RB; Rigaku, Tokyo, Japan) with Cu Kα radiation (λ = 1.5406 Å). Coupled θ–2θ scans were performed with a 2θ step interval of 0.02626° and a scanning speed of 4°/min. For the electrical measurements, the as-sintered samples were polished using silicon carbide paper, and then, the silver paste was painted on both sides of the polished sample surfaces and fired at 550 °C for 30 min. The specimens were poled at room temperature under a dc field of 3 kV/mm for 15 min in a silicone oil bath. The quasi-static d_{33} value was measured by using a quasi-static piezoelectric constant apparatus (YE2730A, Sinocera, Yangzhou, China), and the mechanical quality factor Q_m was determined by a resonance–antiresonance method with an impedance analyzer (Impedance Analyzer PV70A, Beijing, China). Temperature-dependent dielectric properties of samples were measured using an LCR meter (E4980A, Agilent, Santa Clara, CA). The polarization versus electric field (P–E) and strain versus electric field (S–E) curves were measured by using a ferroelectric measuring system (Precision multiferroelectric, Radiant Technologies Inc., Albuquerque, NM) with an accessory laser interferometer vibrometer (AE SP-S 120E, SIOS technic, GmbH, Ilmenau, Germany). The measurement frequency of both the P–E and S–E curves was fixed at 10 Hz. The X-ray photoelectron spectrum (XPS) with a Physical Electronics PHI 5802 using Kα line of Al (hv = 1486.6 eV) as X-ray source was recorded to observe the binding state of manganese in the specimens. The Hitachi F-4600 fluorescence spectrophotometer with the scanning speed of 240 nm/min was used to measure the emission spectra for determining the oxygen vacancy concentration.

Results and discussion

Figure 1a shows the room temperature XRD patterns of BCTZ ceramics with different MnO_2 contents. All samples exhibit a pure perovskite structure without any trace of secondary phase. However, the $(200)_C$ peaks show an obvious splitting corresponding to the $(002)_T/(200)_T$ doublet as shown in Fig. 1b because the selected BCTZ matrix is located at the tetragonal-rich side of tetragonal-orthorhombic phase boundary [10]. With the increase in the MnO_2 content, Fig. 1b, c shows that both (111)c and (200)c reflections exhibit a slight shift toward low angle side until $x = 0.75$, beyond which an abnormal shift toward high angle side can be observed. This suggests that the addition of a small amount of MnO_2 can induce a slight lattice expansion initially, whereas a slight lattice shrinkage can be occurred at the relatively high MnO_2 content.

Figure 2 shows the XPS spectra of Mn $2p_{3/2}$ orbit for $x = 0.25$, 0.75 and 1.25 samples, which was fitted with Gaussian distribution curves. Two distinct components around the ~ 640 eV and 641.5 eV can be assigned as Mn^{2+} and Mn^{3+} ions in $2p_{3/2}$ state, respectively [30]. This should be related to a fact that the valence of Mn ions tends to decrease with increasing temperature and it suggests that only Mn^{2+} and Mn^{3+} ions can be existed in the sample after sintering at the high temperature [31]. Similarly, Yao et al. also found that only Mn^{2+} and Mn^{3+} ions can be detected in PZT- and NKN-based ceramics [32]. With increasing the MnO_2 content, although the divalent Mn^{2+} ions are dominant in the studied composition range, the overall integral intensities corresponding to the Mn^{2+} and Mn^{3+} ions increase monotonically. In addition, the Mn^{2+}/Mn^{3+} ratio also shows a slight increase due to the change of the relative integral intensity between them. Considering that the radius of Mn^{2+} ions is larger than that of Mn^{3+}, Ti^{4+} and Zr^{4+} ions (CN = 6, $R_{Mn^{2+}} = 0.83$ Å, $R_{Mn^{3+}} = 0.645$ Å, $R_{Ti^{4+}} = 0.605$ Å, $R_{Zr^{4+}} = 0.72$ Å), and the radius of Mn^{2+} and Mn^{3+} ions is smaller than that of Ba^{2+} and Ca^{2+} ions (CN = 12, $R_{Mn^{2+}} = 1.22$ Å, $R_{Mn^{3+}} = 1.03$ Å, $R_{Ba^{2+}} = 1.61$ Å, $R_{Ca^{2+}} = 1.34$ Å) [33], it is suggested that Mn ions tend to enter the B-site until $x = 0.75$, beyond which they preferentially enter the A-site. This induces the observed lattice expansion and shrinkage in the relatively low and high MnO_2 content range, respectively.

This also can be confirmed by the Raman spectra. Figure 3 shows the room temperature Raman spectra of BCTZ ceramics with different MnO_2 contents. No obvious change of the vibrational modes except for the modes corresponding to the $A_1(TO_1)$, $E(TO_2)$ and $A_1(LO_3)/E(TO_3)$. The modes of $A_1(TO_1)$ and $E(TO_2)$ are assigned to B–O bonds, while the mode of $A_1(LO_3)/E(TO_3)$ is attributed to the A–O bonds [34–36]. It is evident that with increasing x, both $A_1(TO_1)$ and $E(TO_2)$ modes exhibit a slight weakness at $x \leq 0.75$, which should be resulted from the local structural disorder after the substitution of Mn ions for the B-site ions. However, the peak intensity of these two modes exhibit a slight increase with further increasing x ($x > 0.75$), possibly because Mn ions tend to enter A-site rather than the B-site. Figure 3 shows that the peak intensity of $A_1(LO_3)/E(TO_3)$ mode related to the A–O bonds also exhibits a slight increase, since Mn ions preferentially occupy the A-site as $x > 0.75$.

It is expected that the substitution of Mn ions for B-site Ti/Zr ions can induce the oxygen vacancies

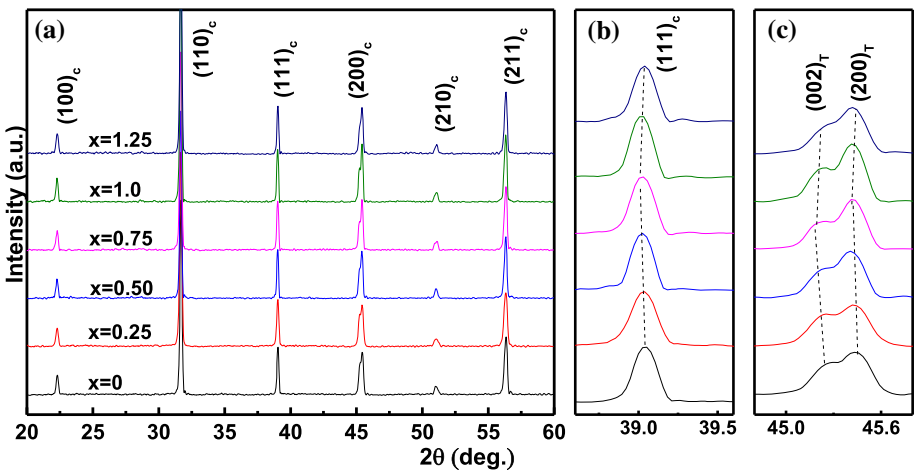

Figure 1 **a** Room temperature XRD patterns of BCTZ ceramics and the enlarged **b** $(111)_c$ and **c** $(200)_c$ reflections with different MnO_2 contents.

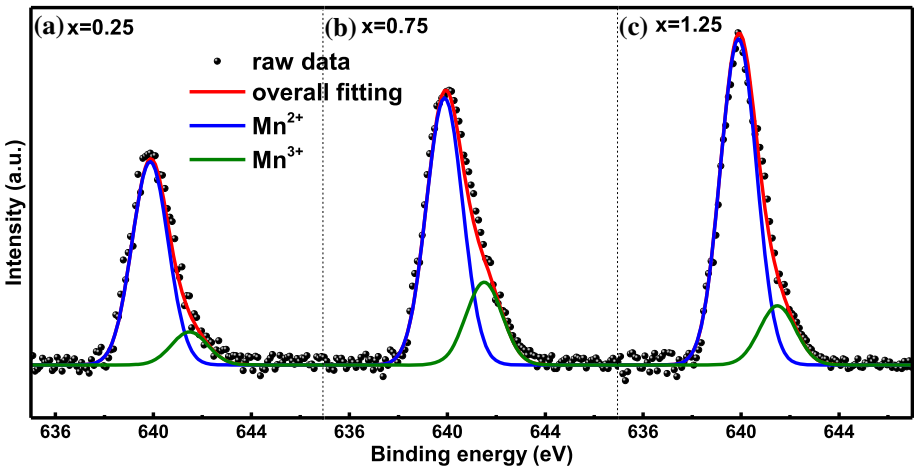

Figure 2 X-ray photoelectron spectroscopy analysis of the Mn $2p_{3/2}$ orbit of the BCTZ ceramics with different MnO_2 content. The dots represent the experimental data, while solid lines represent the fitting data.

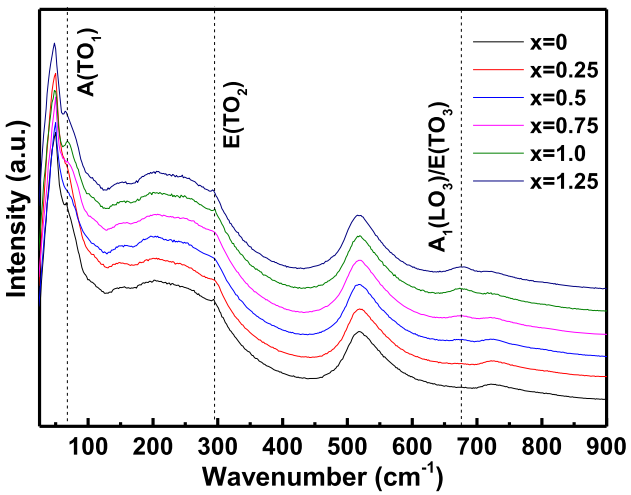

Figure 3 Room temperature Raman spectra of BCTZ ceramics with different MnO_2 contents.

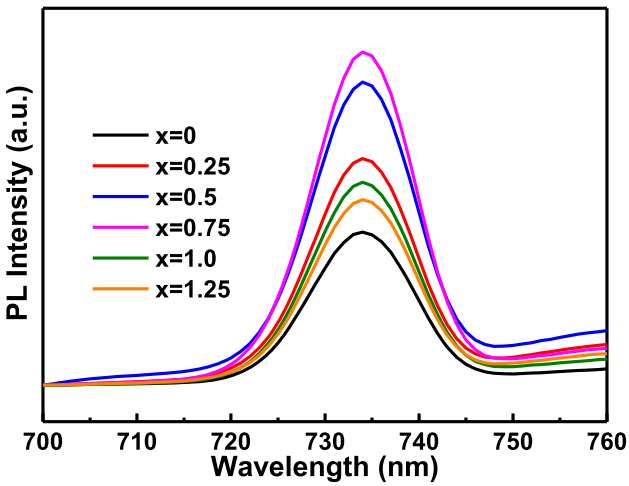

Figure 4 Variation of PL spectra of BCTZ ceramics as a function of x.

due to the charge compensation, which can further form the defect dipole with the negatively charged defects (i.e., impurity Mn defects) and play an important role in various electrical properties. The existence of oxygen vacancies can be detected by photoluminescence (PL) spectra. Figure 4 shows the PL spectra of BCTZ ceramics with different MnO_2 contents. Generally, the PL intensity shows a monotonic increase with increasing the oxygen vacancy content [37]. Very interestingly, with increasing x, the PL intensity exhibits an obvious increase as $x \leq 0.75$. This indicates that the substitution of Mn^{2+}/Mn^{3+} ions for Ti/Zr ions in this composition range is the typical acceptor doping, which can induce the oxygen vacancies. However, with further increasing x, the PL intensity shows an obvious decrease, possibly because Mn ions preferentially occupy the A-site to replace the Ba/Ca ions, which can be considered as the donor doping and is beneficial for restricting the formation of oxygen vacancies.

Figure 5 shows the temperature-dependent relative dielectric constant of BCTZ ceramics with different MnO_2 contents measured at 1 kHz. It can be seen that the temperature corresponding to the dielectric maximal (T_m) shows no obvious change with increasing MnO_2 content until $x = 0.75$, beyond which T_m exhibits a slight decrease. It is usually believed that B-site acceptor doping shows no obvious effect on the T_m value, whereas the A-site donor doping can decrease the T_m value significantly [38–40]. The decrease in the T_m value after the A-site donor doping should be attributed to the local relaxation induced by the cation vacancies. This leads to the distortion of nearby BO_6 octahedron and thus

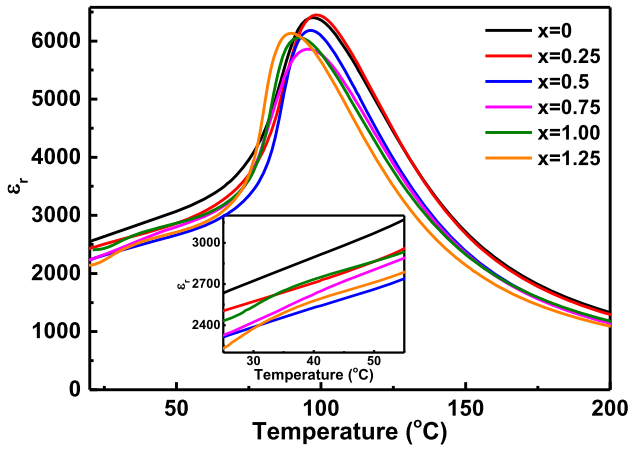

Figure 5 Temperature-dependent relative dielectric constant ε_r (ε_r–T) of BCTZ ceramics with different MnO_2 contents. The inset shows the evolution of ε_r–T curves around the room temperature.

is responsible for the decrease in the T_m value [38]. In addition, it can be seen that the decrease in T_m at $x > 0.75$ is accompanied by the slight shift of the orthorhombic–tetragonal polymorphic phase transition (PPT) temperature toward high temperature range, as shown in the inset of Fig. 5. It is thus suggested that the observed soft behavior at $x > 0.75$ can be attributed to the synergistic effect of the occupation site change of Mn ions and the coexistence of orthorhombic and tetragonal phases.

The electric field-induced polarization (P–E) and strain (S–E) curves of poled BCTZ ceramics with different MnO_2 content at room temperature are displayed in Fig. 6. All samples exhibit the typical square-like P–E loops, and both the maximal polarization (P_{max}) and the remanent polarization (P_r) show little composition dependence, as clearly shown in Fig. 7a. However, it can be found that the P–E loops become increasingly asymmetric with increasing x, as characterized by the separation of the absolute value between the positive coercive field ($+E_c$) and the negative coercive field ($-E_c$). This indicates the existence of an internal bias field (E_i) that defined as the difference between the value of $+E_c$ and the absolute value of $-E_c$. Very interestingly, Fig. 7b shows that the E_i value exhibits an obvious increase until $x = 0.75$, beyond which it shows a slight decrease with further increasing x. This is in good agreement with the variation trend of oxygen vacancy content. Of particular importance is that the appearance of the E_i is accompanied by a distinct change of the strain characteristics. The typical symmetric butterfly-like S–E curves become more and more asymmetric after the MnO_2 doping, which is associated with the gradual decrease in the negative strain. As a result, only a highly asymmetric sprout-shaped strain loop can be observed at $x = 0.075$ with the maximal strain value of $\sim$0.242 under 2 kV/mm, which is $\sim$82% higher than the undoped sample (only $\sim$0.133% at $x = 0$). Figure 7c shows that the corresponding large signal d_{33}* (= S_{max}/E_{max}) value also exhibits an obvious increase from only $\sim$ 665 pm/V at $x = 0$ to 1210 pm/V at $x = 0.75$. Such a high d_{33}* value has been rarely reported in BT-based ceramics under such a high external electric field amplitude, suggesting that the present studied composition exhibits a good potential for applications in actuators. Figure 7d displays the evolution of the small signal quasi-static d_{33} value and the mechanical quality factor Q_m, and these two parameters exhibit an opposite trend. With increasing x, the d_{33} value exhibits a slight decrease with increasing x, while the Q_m value shows a slight increase. This is the typical characteristic of hardening effect. The largest Q_m and the lowest d_{33} value can be observed at $x = 0.75$ sample. Very interestingly, no negative strain can be observed in the corresponding strain curve. These phenomena should be undoubtedly related to the E_i established by the defect dipoles between oxygen vacancy and the acceptor doping Mn ions. After poling, the defect dipoles can be oriented along the poling field direction, acting as the pinning center to restrict the domain switching. As a result, if the external electric field direction is reversed, these preferentially oriented domains cannot be switched parallel to the reversed field direction. This also induces the observed asymmetric P–E loops. However, owing to the restriction of the preferentially oriented defect dipoles, the P_r value exhibits little composition dependence as shown in Fig. 7a. With further increasing x, an obvious soft behavior can be observed as characterized by the appearance of negative strain, the reduction in the asymmetry of S–E curves, the increase in the d_{33} value, the decrease in the Q_m, etc., possibly because Mn ions tend to enter A site and the orthorhombic–tetragonal PPT temperature is shifted toward room temperature.

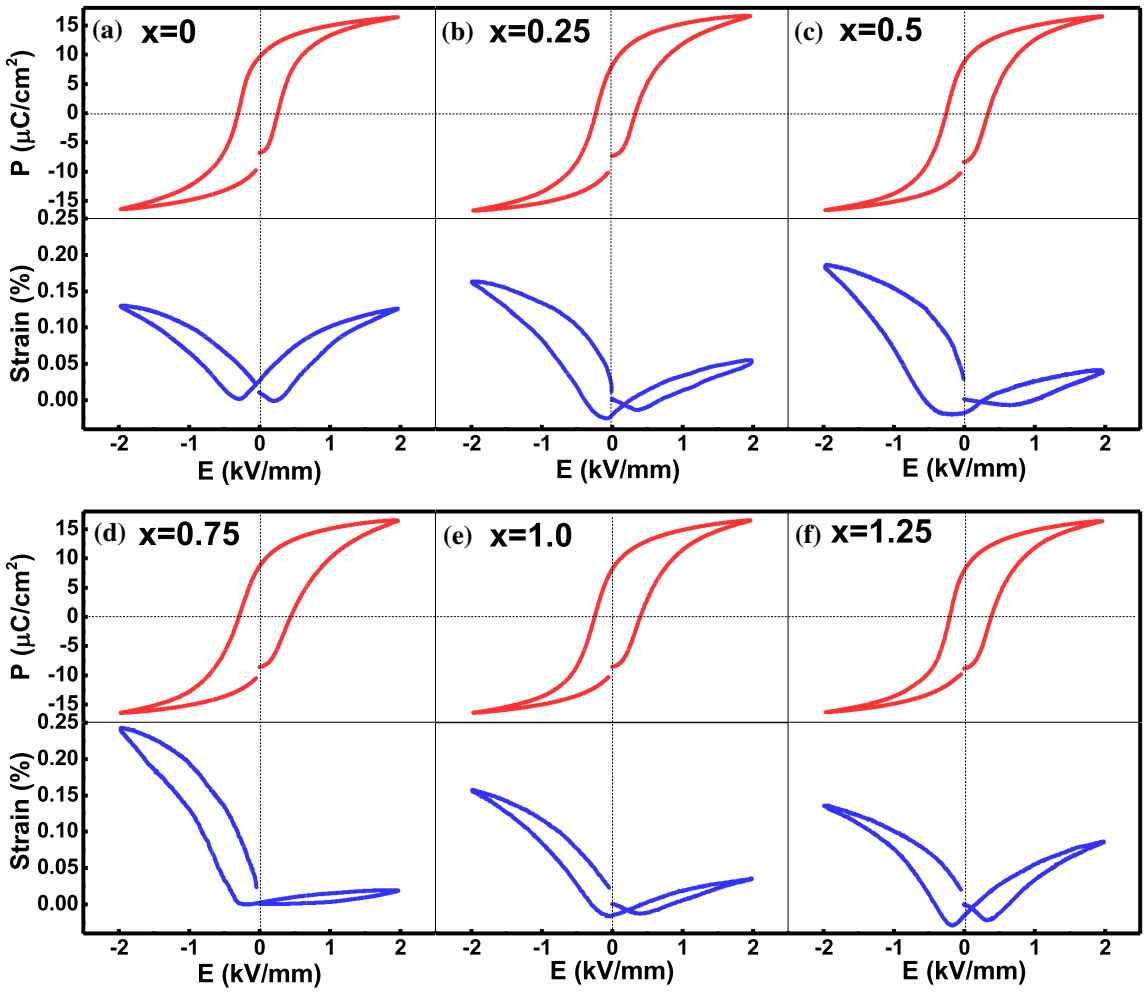

Figure 6 Evolution of the bipolar *P–E* loops and *S–E* curves of BCTZ ceramics as a function of x measured at room temperature with the field amplitude of 2 kV/mm.

Conclusions

In summary, the influence of the MnO_2 doping on phase structure and various electrical properties of BCTZ ceramics was investigated. It is found that a small amount of MnO_2 can enter the B site to act as the acceptor defect center, leading to the formation of oxygen vacancies due to the charge compensation. After poling, the defect dipoles between the negatively charged defects and the oxygen vacancies can orient along the poling field direction, leading to the asymmetric but recoverable *S–E* curves. This induces an obvious enhancement of strain value and an ultrahigh electrostrain with a value of 0.242% (d_{33}* = 1210 pm/V) at 2 kV/mm can be achieved in 0.75 mol% MnO_2-doped BCTZ ceramics. However, with further increasing MnO_2 content, an obvious soft behavior can be observed because of the occupation site change of Mn ions and the *O–T* phase coexistence. This study provides a good strategy for achieving ultrahigh strains in modified BT-based ceramics via defect engineering.

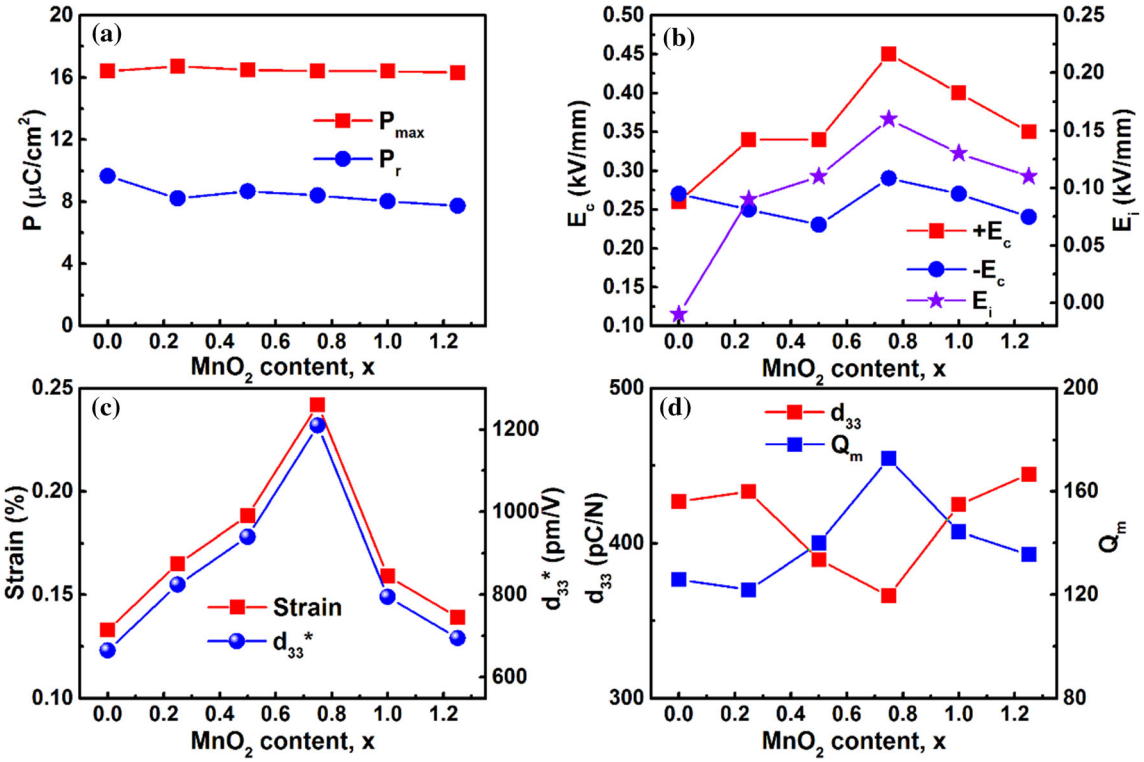

Figure 7 Evolution of various electrical parameters as a function of *x*.

Acknowledgements

This work was supported by the National Natural Science Foundation of China (Grant Nos. 52072103 and U19A2087), Hubei Key Laboratory of Ferro- & Piezoelectric Materials and Devices (Grant No. K202002) and Project of College Students' Innovation and Entrepreneurship Training Program (Grant No. 202010359012).

Declarations

Conflict of interest The authors declare that they have no known competing financial interests or personal relationships that could have appeared to influence the work reported in this paper.

References

[1] Zhang ST, Kounga AB, Jo W, Jamin C, Seifert K, Granzow T, Rodel J, Damjanovic D (2009) High-strain lead-free antiferroelectric electrostrictors. Adv Mater 21:4716–4720. https://doi.org/10.1002/adma.200901516

[2] Hao JG, Shen B, Zhai JW, Liu CZ, Li XL, Gao XY (2013) Switching of morphotropic phase boundary and large strain response in lead-free ternary $(Bi_{0.5}Na_{0.5})TiO_3$-$(K_{0.5}Bi_{0.5})$-TiO_3-$(K_{0.5}Na_{0.5})NbO_3$ system. J Appl Phys. https://doi.org/10.1063/1.4795511

[3] Shi J, Fan HQ, Liu X, Bell AJ (2014) Large electrostrictive strain in $(Bi_{0.5}Na_{0.5})TiO_3$-$BaTiO_3$-$(Sr_{0.7}Bi_{0.2})TiO_3$ solid solutions. J Am Ceram Soc 97:848–853. https://doi.org/10.1111/jace.12712

[4] Uiiah A, Ahn CW, Uiiah A, Kim W (2013) Large strain under a low electric field in lead-free bismuth-based piezoelectrics. Appl Phys Lett. https://doi.org/10.1063/1.4813420

[5] Liu WF, Ren XB (2009) Latge piezoelectric effect in Pb-free ceramics. Phys Rev Lett. https://doi.org/10.1103/PhysRevLett.103.257602

[6] Tian Y, Wei LL, Chao XL, Liu ZH, Yang ZP (2013) Phase transition behavior and large piezoelectricity near the morphotropic phase boundary of lead-free $(Ba_{0.85}Ca_{0.15})(Zr_{0.1}$-$Ti_{0.9})O_3$ ceramics. J Am Ceram Soc 96:496–502. https://doi.org/10.1111/jace.12049

[7] Wang D, Jiang ZH, Yang B, Zhang ST, Zhang MF, Guo FF, Cao WW (2014) Phase diagram and enhanced piezoelectric response of lead-free $BaTiO_3$-$CaTiO_3$-$BaHfO_3$ system. J Am Ceram Soc 97:3244–3251. https://doi.org/10.1111/jace.13137

[8] Zhao CL, Wu HJ, Li F, Cai YQ, Zhang Y, Song DS, Wu JG, Lyu X, Yin J, Xiao DQ, Zhu JG, Pennycook SJ (2018)

Practical high piezoelectricity in barium titanate ceramics utilizing multiphase convergence with broad structural flexibility. J Am Chem Soc 140:15252–15260. https://doi.org/10.1021/jacs.8b07844

[9] Wang DW, Fan ZM, Rao GH, Wang G, Liu Y, Yuan CL, Ma T, Li DJ, Tan XL, Lu ZL, Feteira A, Liu SY, Zhou CR, Zhang SJ (2020) Ultrahigh piezoelectricity in lead-free piezoceramics by synergistic design. Nano Energy. https://doi.org/10.1016/j.nanoen.2020.104944

[10] Yang ZJ, Fu J, Xu YD, Zuo RZ (2021) Field-insensitive giant dynamic piezoelectric response and its structural origin in (Ba, Ca)(Ti, Zr)O3 tetragonal-orthorhombic phase-boundary ceramics. J Eur Ceram Soc 41:6441–6448. https://doi.org/10.1016/j.jeurceramsoc.2021.06.004

[11] Zhao CL, Wu B, Thong HC, Wu JG (2018) Improved temperature stability and high piezoelectricity in lead-free barium titanate-based ceramics. J Eur Ceram Soc 38:5411–5419. https://doi.org/10.1016/j.jeurceramsoc.2018.08.004

[12] Mayamae J, Vittayakorn W, Sukkhab U, Bongkarnc T, Muanghluae R, Vittayaakorn N (2017) High piezoelectric response in lead free $0.9BaTiO_3$-(0.1-x)$CaTiO_3$-x$BaSnO_3$ solid solution. Ceram Int 43:S121–S128. https://doi.org/10.1016/j.ceramint.2017.05.252

[13] Chaiyo N, Cann DP, Vittayakorn N (2015) Phase transitions, ferroelectric, and piezoelectric properties of lead-free piezoelectric x$BaZrO_3$-(0.25-x)$CaTiO_3$-0.75$BaTiO_3$ ceramics. J Mater Sci 50:6171–6179. https://doi.org/10.1007/s10853-015-9174-y

[14] Wang XF, Chao XL, Liang PF, Wei LL, Yang ZP (2014) Polymorphic phase transition and enhanced electrical properties of $(Ba_{0.91}Ca_{0.09-x}Sr_x)(Ti_{0.92}Sn_{0.08})O_3$ lead-free ceramics. Ceram Int 40:9389–9394. https://doi.org/10.1016/j.ceramint.2014.02.008

[15] Acosta M, Novak N, Jo W, Rodel J (2014) Relationship between electromechanical properties and phase diagram in the $Ba(Zr_{0.2}Ti_{0.8})O_3$–x$(Ba_{0.7}Ca_{0.3})TiO_3$ lead-free piezoceramics. Acta Mater 80:48–55. https://doi.org/10.1016/j.actamat.2014.07.058

[16] Zhu LF, Zhang BP, Zhao L, Li JF (2014) High piezoelectricity of $BaTiO_3$-$CaTiO_3$-$BaSnO_3$ lead-free ceramics. J Mater Chem C 2:4764–4771. https://doi.org/10.1039/C4TC00155A

[17] Zhu LF, Zhang BP, Zhao XK, Zhao L, Yao FZ, Han X, Zhou PF, Li JF (2013) Phase transition and high piezoelectricity in (Ba, Ca)$(T_{i1-x}S_nx)_O3$ lead-free ceramics. Appl Phys Lett. https://doi.org/10.1063/1.4818732

[18] Ehmke MC, Ehrlich SN, Blendell JE, Bowman KJ (2012) Phase coexistence and ferroelastic texture in high strain (1–x)$Ba(Zr_{0.2}Ti_{0.8})O_{3-x}(Ba_{0.7}Ca_{0.3})TiO_3$ piezoceramics. Appl Phys Lett 111:124–110. https://doi.org/10.1063/1.4730342

[19] Zhang MH, Liu YX, Wang K, Koruza J, Schultaeiβ J (2020) Origin of high electromechanical properties in (K, Na)NbO_3-based lead-free piezoelectric modified with $BaZrO_3$. Phys Rev Mater. https://doi.org/10.1103/PhysRevMaterials.4.064407

[20] Fu J, Zuo RZ, Qi H, Chan TS (2019) Identifying the local defect structure in $(Na_{0.5}K_{0.5})NbO_3$: 1mol% CuO lead-free ceramics by X-ray absorption spectra. Appl Phys Lett 114:92–904. https://doi.org/10.1063/1.5088397

[21] Eichel RA, Erhart P, Traskelin P, Albe K, Kungl H, Hoffmann MJ (2008) Defect-dipole formation in copper-doped $PbTiO_3$ ferroelectrics. Phys Rev Lett. https://doi.org/10.1103/PhysRevLett.100.095504

[22] Eichel RA (2007) Defect structure of oxide ferroelectrics-valence state, site of incorporation, mechanisms of charge compensation and internal bias fields. J Electroceram 19:9–21. https://doi.org/10.1007/s10832-007-9068-8

[23] Zhang SJ, Lim JB, Lee HJ, Shrout TR (2009) Characterization of hard piezoelectric lead-free ceramics. IEEE Trans Ultrason Ferroelectr Freq Control 56:1523–1527. https://doi.org/10.1109/TUFFC.2009.1215

[24] Zho ZH, Lv YK, Dai YJ, Zhang SJ (2020) Ultrahigh electrostrain in acceptor-doped KNN lead-free piezoelectric ceramics via defect engineering. Acta Mater 200:35–41. https://doi.org/10.1016/j.actamat.2020.08.073

[25] Liu XM, Tan XL (2016) Giant strains in non-texture $(Bi_{1/2}Na_{1/2})TiO_3$-based lead-free ceramics. Adv Mater 28:574–578. https://doi.org/10.1002/adma.201503768

[26] Cao WP, Li WL, Feng Y, Bai T, Qiao YL, Hou YF, Zhang TD, Yu Y, Fei WD (2016) Defect dipole induced large recoverable strain and high energy-storage density in lead-free $Na_{0.5}Bi_{0.5}TiO_3$-based systems. Appl Phys Lett 108:202902. https://doi.org/10.1063/1.4950974

[27] Fu J, Zuo RZ (2012) Polarization reversal and dynamic scaling of $(Na_{0.5}K_{0.5})NbO_3$ lead-free ferroelectric ceramics with double hysteresis-like loops. J Appl Phys 112:104114. https://doi.org/10.1063/1.4768270

[28] Ren XB (2004) Large electric-field-induced strain in ferroelectric crystals by point-defect-mediated reversible domain switching. Nat Mater 3:91–94. https://doi.org/10.1038/nmat1051

[29] Zhang LX, Chen W, Ren X (2004) Large recoverable electrostrain in Mn-doped (Ba, Sr)TiO_3 ceramics. Appl Phys Lett 85:5658–5660. https://doi.org/10.1063/1.1829394

[30] Nageri M, Kumar V (2018) Manganese-doped $BaTiO_3$ nanotube arrays for enhanced visible light photocatalytic applications. Mater Chem Phys 213:400–405. https://doi.org/10.1016/j.matchemphys.2018.04.003

[31] Ng YS, Alexander SM (1983) Structural studies of manganese stabilized lead-zirconate-titanate. Ferroelectrics 51:81–86. https://doi.org/10.1080/00150198308009056

[32] Yao FZ, Zhang MH, Wang K, Zhou JJ, Chen F, Xu B, Li F, Shen Y, Zhang QH, Gu L, Zhang XW, Li JF (2018) Refreshing piezoelectrics: distinctive role of manganese in lead-free perovskites. ACS Appl Mater Interfaces 10:37298–37306. https://doi.org/10.1021/acsami.8b14958

[33] Shannon RD (1976) Revised effective ionic radii and systematic studies of interatomic distances in halides and chalcogenides. Acta Cryst A 32:751–767. https://doi.org/10.1107/S0567739476001551

[34] Damjanovic D, Biancoli A, Batooli L, Vahabzadeh A, Trodahl J (2012) Elastic, dielectric, and piezoelectric anomalies and Raman spectroscopy of $0.5Ba(Ti_{0.8}Zr_{0.2})O_3$–$0.5(Ba_{0.7}Ca_{0.3})TiO_3$. Appl Phys Lett 100:192–907. https://doi.org/10.1063/1.4714703

[35] Venkata RE, Mahajan A, Graca MPF, Mendiratta SK, Monteiro JM, Valente MA (2013) Structure and ferroelectric studies of $(Ba_{0.85}Ca_{0.15})(Ti_{0.9}Zr_{0.1})O_3$ piezoelectric ceramics. Mater Res Bull 48:4395–4401. https://doi.org/10.1016/j.materresbull.2013.05.108

[36] Pasha UM, Zheng H, Thakur OP, Feteira A, Whittle KR, Sinclair DC (2007) Reaney IM (2007) In situ Raman spectroscopy of A-site doped barium titanate. Appl Phys Lett. https://doi.org/10.1063/1.2768881

[37] Shi YJ, Dong XY, Zhao K, Yang WW, Zhu K, Hu R, Zeng HR, Shen B, Zhai JW (2021) Potential high-temperature piezoelectric ceramics with remarkable performances enhanced by the second-order Jahn-Teller effect. ACS Appl Mater Interfaces 13:14385–14393. https://doi.org/10.1021/acsami.1c00790

[38] Freeman CL, Dawson JA, Harding JH, Ben LB, Sinclair DC (2012) The influence of A-site rare earth ion size in controlling the Curie temperature of $Ba_{1-x}Re_xTi_{1-x/4}O_3$. Adv Funct Mater 23:491–495. https://doi.org/10.1002/adfm.201201705

[39] Sun HJ, Zhang Y, Liu XF, Liu Y, Chen W (2015) Effects of CuO additive on structure and electrical properties of low-temperature sintered $Ba_{0.98}Ca_{0.02}Zr_{0.02}Ti_{0.98}O_3$ lead-free ceramics. Ceram Int 41:555–565. https://doi.org/10.1016/j.ceramint.2014.08.104

[40] Sinclair DC, Attfield JP (1999) The influence of A-cation disorder on the Curie temperature of ferroelectric $ATiO_3$ perovskties. Chem Commun. https://doi.org/10.1039/A903680F